

1 Radiative convective equilibrium over a land
2 surface

3
4 Nicolas Rochetin

5 Columbia University

6 New York, NY 10027

7
8 Benjamin R. Lintner

9 Rutgers, the State University of New Jersey

10 New Brunswick, NJ 08901

11
12 Kirsten L. Findell

13 Geophysical Fluid Dynamics Laboratory

14 Princeton, NJ 08542

15
16 Adam H. Sobel

17 Columbia University

18 New York, NY 10027

19
20 Pierre Gentine¹

21 Columbia University

¹ Corresponding author: Pierre Gentine, Earth Institute - Department of Earth and Environmental Engineering, Columbia University, 500 W 120th st., New York, NY 10027, email: pg2328@columbia.edu

22

23

24

25 Abstract

26

27 Radiative-convective equilibrium (RCE) describes an idealized atmosphere in which the
28 vertical temperature distribution is determined by a balance between radiative and
29 convective fluxes. While RCE has been applied extensively over oceans, its application
30 to land has been limited. The present study explores the properties of RCE over land
31 surfaces, using an atmospheric single column model (SCM) from the Laboratoire de
32 Meteorologie Dynamique (LMD) General Circulation Model (LMDZ5B) coupled in
33 temperature and moisture to a land surface model. Given the presence of a large-
34 amplitude diurnal heat flux cycle, the inclusion of land surface hydrology, and the finite
35 moisture capacity of the surface, the resultant RCE exhibits multiple equilibria when
36 conditions are neither water- nor energy-limited. By varying top-of-the-atmosphere
37 insolation (latitude), total water content, and initial temperature conditions, the sensitivity
38 of the LMDZ5B land region RCE is assessed, with an emphasis on the role of clouds.
39 The presence or absence of low-level clouds and fog as well as the diurnal cycle are
40 required for the existence of multiple equilibria, and have a leading-order impact on the
41 equilibrium states since they strongly modulate the diurnal evolution of surface heating.
42 In addition the simulated surface precipitation rate varies non-monotonically with latitude
43 as a result of a tradeoff between cloud-base rain rate and rain re-evaporation, thus
44 underscoring the importance of subcloud layer processes and unsaturated downdrafts.

45 Overall this analysis suggests the key role of the diurnal evolution of the boundary layer
46 and of low-level clouds over land.

47

48

49

50

51

52

53

54

55 1. Introduction

56

57 The concept of radiative-convective equilibrium (RCE) was first introduced by Manabe
58 and Wetherlad (1967) to describe an idealized, statistical state of the atmosphere in
59 which the vertical temperature distribution is determined by a balance between radiative
60 and convective fluxes. RCE postulates that, on average, convective motions
61 compensate for the destabilization of the atmosphere by radiation. RCE represents a
62 powerful tool for estimating convective sensitivity to surface conditions (temperature and
63 moisture) and diagnosing the possible mechanisms through which deep convection
64 maintains itself in the absence of a large-scale flow. In particular, RCE has been applied
65 to a wide range of problems, including estimation of convective mass fluxes and scaling
66 properties (Tompkins and Craig 1998a), the organization of tropical deep convection
67 (Tompkins and Craig 1998b, Tompkins 2001a,b) and climate sensitivity to greenhouse
68 gas forcing (Muller et al. 2011; Romps 2011) .

69

70 In most of the prior work involving RCE in either single column models (SCM) and in
71 cloud resolving models (CRM), the surface boundary has been an ocean or ocean-like,
72 often with prescribed surface temperature. In the present study, we consider extension
73 of the concept of RCE to a land surface with a closed (water-conserving) hydrologic
74 budget. To our knowledge RCE has not been applied to a land surface beside over a
75 swamp surface (Manabe and Wetherald 1967; Renno 1997). Complications over land
76 stem from the greater complexity associated with interacting soil column components

77 such as vegetation, soil moisture, and soil temperature. Recently, (Tompkins and Craig
78 1998a; Schlemmer et al. 2011) performed an RCE-like experiment involving a CRM
79 coupled to land surface in which a "diurnal equilibrium" state is reached, i.e., a quasi-
80 stationary regime in which the surface and the boundary layer temperatures exhibit
81 diurnal oscillations. In their study, the soil and atmospheric temperature profiles were
82 relaxed toward climatological values at points far from the surface. As far as we are
83 aware, our study is the first to evaluate equilibrium land-atmosphere coupling in a SCM
84 of the atmosphere coupled to a land surface model.

85

86 Of particular interest in our exploration of RCE over land is the potential existence of
87 multiple equilibria. For oceanic, fixed-SST, conditions, the RCE state is uniquely
88 determined by SST and the radiative forcing. That is, in the absence of energy
89 exchange through the surface (and horizontal advection), the isolated, fixed SST RCE
90 system possess a unique equilibrium solution (Hilbert 1912, Tompkins and Craig 1998b;
91 Renno 1997), with the ocean acting as both a thermostat and infinite water reservoir.
92 On the other hand, (Renno 1997, Tompkins 2001a,b) showed that introduction of a
93 surface hydrologic cycle through a swamp ocean, in which the surface temperature is
94 interactively determined through the balance of surface fluxes, assuming zero soil heat
95 capacity, permits the existence of multiple equilibria. Even if multiple equilibria are not
96 realized in the real climate system, e.g., because of the presence of variability resulting
97 from synoptic scale weather systems or seasonal evolution, they may nonetheless
98 provide insights into the direction of evolution of the land-atmosphere system.

99

100 Over land the existence of multiple equilibria has been explored in the context of land-
101 atmosphere feedbacks. For instance, large-scale continental recycling forced by
102 stochastic advection exhibits two distinct equilibria with a dry and moist surface state
103 (Rodríguez-Iturbe et al. 1991a,b; Entekhabi et al. 1992; Muller et al. 2011; Roms 2011).
104 Land and boundary-layer interactions can also induce bimodality in the surface Bowen
105 ratio (Entekhabi and Brubaker 1995; Brubaker and Entekhabi 1995). The Global Land
106 Atmosphere Coupling Experiment (GLACE; Koster et al. 2004) have shown the
107 existence of hotspots of land-atmosphere coupling which typically occur in regions or
108 seasons exhibiting swings between dry and moist conditions. The physical mechanisms
109 in actions at those specific locations are still not well understood, even if some
110 significant progress has been made (Guo et al. 2006; Koster et al. 2006; DelSole et al.
111 2009). It appears that hotspots result from large-scale variability and its interaction with
112 the local climate response to changes in surface Bowen ratio. Recently, (Aleina et al.
113 2013) showed that in a toy model of a desert planet, multiple equilibria emerged with the
114 inclusion of vegetation dynamics.

115

116 Apart from the GCM-based analyses of GLACE most studies of the feedbacks of soil
117 moisture and precipitation over land have been performed over relatively short time
118 scales from one to several days (Hohenegger et al. 2009; Seneviratne et al. 2010;
119 Findell et al. 2011; Gentine et al. 2013). On the other hand, the characterization of the
120 coupling and feedbacks between the land and the atmosphere on long timescales
121 remains limited. A key challenge, in both observations and complex GCMs, is that
122 variability associated with other climate system processes may mask signatures of land-

123 atmosphere coupling. Thus, we believe that analyses performed using idealized set-ups
124 such as the model considered here can stimulate improved understanding of long-term
125 land-atmosphere interactions: what such analyses may lack in terms of realism is
126 leveraged against the ease and transparency of diagnosis.

127

128 The paper is structured as follows. Section 2 provides an overview of the Laboratoire de
129 Meteorologie Dynamique (LMD) General Circulation Model (LMDZ5B) SCM used in this
130 study and the experimental setup employed to obtain RCE solutions over land. In
131 section 3, we document the existence of multiple equilibria in a set of experiments in
132 which we vary latitude, total moisture content, and initial soil temperature, while Section
133 4 provides a more in-depth analysis of RCE solution behaviors and how these relate to
134 land surface, cloud-radiative, and convective processes in the model. In section 5, we
135 present the results of sensitivity experiments to assess how the diurnal cycle of
136 radiation and cloud radiative feedbacks impact the existence of multiple equilibria. The
137 final section summarizes the key findings of this study and discusses some implications
138 of land region RCE for interpreting land region climate.

139

140 2. Model description and setup:

141 *2a. Model description:*

142 **2a1. ATMOSPHERE**

143 We use the SCM version of the LMDZ5B GCM developed by the Laboratoire de
144 Meteorologie Dynamique (Hourdin et al. 2012). LMDZ5B has been used to perform

145 climate simulations for the IPCC 5th assessment report. Here we describe the main
146 structure of the model; the reader is referred to (Hourdin et al. 2012) for a more
147 extensive discussion.

148

149 The model has 39 levels in the vertical, with the grid stretched near the surface. Thus,
150 the first grid point is at 35 m, with 8 grid-points in the first kilometer. Between 1 and 20
151 km, the mean vertical resolution is 800 m. The model top is located at 40 km. The
152 model contains separate treatments of shallow and deep convection. For shallow
153 convection, the eddy diffusive scheme of Mellor and Yamada (1994) is combined with a
154 mass-flux representation of boundary-layer thermals (Hourdin et al. 2002; Rio and
155 Hourdin 2008; Rio et al. 2010) to account for, respectively, the turbulence in the surface
156 layer and in the inversion and the non-local convective transport induced by coherent
157 structures of the boundary layer. The thermal model uses a bulk entraining-detraining
158 plume approach (Simpson and Wiggert 1969; Betts 1973) to compute the properties of
159 a mean characteristic thermal representing the dry and cloudy (if saturation level is
160 reached) boundary-layer thermals present in a model grid-cell. The plume model is
161 used to diagnose the height of the cumulus base and top, as well as the vertical profiles
162 of the plume vertical velocity, thermodynamic properties and fractional coverage,
163 through the mass flux vertical evolution. Emanuel's (Emanuel 1991) deep convection
164 scheme is added to this scheme for the treatment of precipitating-deep convection. The
165 scheme has been modified by (Grandpeix and Phillips 2004) to improve the sensitivity
166 of the simulated deep convection to tropospheric relative humidity (Derbyshire et al.
167 2004). The triggering criterion of deep convection is based on the concept of available

168 lifting energy (ALE) provided by thermals. Deep convection is triggered whenever ALE
169 overcomes the Convective INhibition (CIN). A cold pool (or wake) parameterization has
170 also been added to Emanuel's scheme. The cold pools are fed by the unsaturated
171 downdrafts resulting from rain evaporation (Betts 1976; Tompkins 2001b). These cold
172 pools provide a lifting energy for updrafts that may help re-trigger deep convection by
173 exceeding the CIN (Tompkins 2001b). Ultimately, both thermals and cold pools
174 (subcloud processes) provide independent lifting energies, which are compared to the
175 CIN to decide whether deep convection is triggered. The closure hypothesis suggested
176 by Grandpeix and Lafore (2010) relates the cloud-base mass flux (M_b) to the available
177 lifting power (ALP) provided by subcloud processes (thermals and cold pools), the
178 convective inhibition and the vertical velocity at the level of free convection (see details
179 in Grandpeix et al. 2010; Grandpeix and Lafore 2010).

180

181 Cloud cover in the deep convective scheme is based on a statistical cloud scheme with
182 a log-normal probability density function to determine subgrid scale total cloud water
183 content (Bony and Emanuel 2001). The latent heat of melting of ice is not taken into
184 account in the convective parameterization. Precipitation is divided into (i) a convective
185 part, generated by Emanuel's convection scheme, and a (ii) stratiform part, generated
186 by large-scale condensation processes that occur when the average relative humidity of
187 the grid reaches saturation. Similar to moist convection, the large-scale processes heat
188 the atmosphere and create clouds. The radiation scheme (Morcrette 1991) fully
189 interacts with clouds and all other components of the atmosphere except aerosols.

190 **2a2. SOIL MODEL**

191 The soil model uses a diffusion scheme for heat propagation, assuming an effusivity,
 192 the square root of the product of the thermal conductivity and volumetric heat capacity,
 193 of $\varepsilon = 2000 \text{ W}/(\text{m}^2 \cdot \text{s}^{0.5})$. A zero ground heat flux hypothesis is imposed at infinite depth.
 194 The surface albedo is taken as $\alpha = 0.19$. Soil water content Q_{soil} (or soil moisture)
 195 dynamics is represented with a simple “bucket” model (Koster and Suarez 1994). There
 196 is no explicit representation of the vegetation. The evolution of Q_{soil} is computed from the
 197 balance between precipitation and evaporation and runoff generation. A soil saturation
 198 threshold is prescribed at $Q_{\text{max}}=150 \text{ mm}$, above which the excess of water is evacuated
 199 as runoff. This threshold corresponds to an effective rooting depth (Rodríguez-Iturbe et
 200 al. 1999; Laio et al. 2001).

201 **2a3. SURFACE FLUXES**

202 The sensible heat flux and evaporation are computed via the bulk formulations:
 203 $\phi_{\text{sens}} = \rho V_0 C_{d,v} C_{d,h} (T_s - T_1)$ and $Evap = \beta \rho V_0 C_{d,v} C_{d,h} (q_{\text{sat},T_s} - q_1)$. Here, $\rho = 1.17 \text{ kg}/\text{m}^3$ is the
 204 surface air density, V_0 the first level wind speed, $C_{d,v} = 0.001$ the neutral drag coefficient
 205 for a land surface, $C_{d,h}$ the stability correction based on a local Richardson number (see
 206 Hourdin et al. 2012), β the evapotranspiration coefficient, i.e. the ratio between effective
 207 evaporation and potential evaporation, T_s the surface skin temperature, T_1 the first
 208 atmospheric layer temperature, q_{sat,T_s} the saturation specific humidity at the surface, and
 209 q_1 the first layer specific humidity. If $Q_{\text{soil}} \leq Q_{\text{max}} / 2$ β depends linearly on the ratio of Q_{soil}
 210 and Q_{max} , $\beta = 2Q_{\text{soil}} / Q_{\text{max}}$ otherwise $\beta = 1$. This relationship actually mimics idealized
 211 vegetation, for which the stomatal opening linearly depends on soil moisture, until it
 212 reaches a maximum value (saturation) (Porporato et al. 2001).

213 **2b. Methodology:**

214 The SCM is integrated for 10 years with a timestep $\Delta t = 450\text{s}$ (the LMDZ standard
215 timestep used for CMIP5). An initial atmospheric profile is prescribed, as well as an
216 initial vertically-uniform ground temperature T_0 and soil moisture Q_0 . The radiative-
217 convective equilibrium (RCE) framework is used without large-scale velocity nor
218 tendencies. The 1D soil-atmosphere system is thus closed and only exchanges energy
219 with space. If soil moisture is below the maximum water holding capacity $Q_{soil} \leq Q_{max}$, no
220 runoff is generated and the total water quantity is conserved: $Q_{TOT} = Q_{soil} + W$, where W
221 is the precipitable water. A diurnal cycle of incoming shortwave flux at the top of the
222 atmosphere (TOA) is imposed and its maximum value corresponds to the annual mean
223 flux met at the prescribed latitude. The seasonal cycle is removed for simplicity.

224

225 The sensitivity experiments discussed in the following sections address changes in (i)
226 latitude, λ ; (ii) total water content, Q_{TOT} ; and (iii) initial ground temperature, T_0 . Note that
227 variation in total water content Q_{TOT} is performed by varying the initial ground water
228 content Q_0 while maintaining the same initial atmospheric profile.

229

230 **2c. Characteristics of the baseline LMDZ5B RCE state:**

231 The atmosphere is in RCE when the atmospheric radiative cooling balances convective
232 fluxes. Since radiation and convection experience a diurnal cycle, we define the
233 equilibrium in terms of a 10-day moving average in order to smooth the diurnal cycle
234 and possible day-to-day variations in precipitation. We run the model for the following

235 baseline conditions: $\lambda = 35^\circ$, $T_0 = 300\text{K}$, $Q_{TOT} = 40\text{mm}$. In this case, the RCE is reached in
236 less than a year. The time scale of convection is much faster than the radiative time
237 scale so that any fluctuations in the surface and TOA energy balances are effectively
238 simultaneous. Even though the soil-atmosphere thermodynamic system is not strictly in
239 equilibrium with space (since net TOA radiation is nonzero), convection renders the
240 atmosphere in approximate equilibrium; thus, on short timescales, it is possible for the
241 entire land-atmosphere system to be out of equilibrium even as the atmosphere itself is
242 effectively in equilibrium. However, the RCE guarantees the same energy imbalance at
243 the surface and at TOA. On longer time scale (~ 10 years) and at final equilibrium the
244 net TOA flux vanishes.

245

246 The soil model in the LMDZ5B SCM may be compared with a slab ocean model with a
247 small heat capacity, which allows diurnal variations in surface temperature, but with a
248 finite water holding capacity. Because of the small soil inertia the system oscillates
249 around the equilibrium state on daily timescales. This diurnal cycle provides increased
250 surface variability compared to the oceanic case. This is a difference with the oceanic
251 case: even at equilibrium there can be substantial subdiurnal changes in surface
252 temperature, boundary layer dynamics, cloud cover, convection, which are potentially
253 nonlinearly responding to the diurnal course of radiation. This added variability can
254 potentially be important to reach a global extremum as opposed to a local extremum
255 (Rodriguez-Iturbe et al. 1991), as will be seen in section 5.

256

257 The addition of the surface hydrological cycle also increases the system's degrees of
258 freedom compared to the oceanic case while the closed hydrologic cycle imposes the
259 total amount of water in the system. Runoff was negligible in our simulations with the
260 relatively deep soil layer (1.5m) chosen. Compared to the oceanic counterpart, the
261 surface is not an infinite source of water. The energy in the system is thus controlled by
262 the latitude (and planetary albedo) and the hydrologic cycle is constrained by the initial
263 total water content.

264

265 Fig 1 highlights the mean-diurnal cycle at equilibrium over the last 3 months of the
266 simulation. The surface and TOA energy budgets are close to zero in the baseline
267 simulation. The land region RCE has reached a steady periodic regime, in which the
268 diurnal solar forcing drives a periodic response of the land-atmosphere system, both in
269 terms of surface temperature and precipitation as seen in Fig 1a and b. At equilibrium,
270 surface temperature and precipitation exhibit very little day-to-day variability (not shown).
271 The diurnal cycle of T_s exhibits a 1- to 2-hour lag with respect to solar forcing, which is
272 characteristic of continental precipitation (Gentine et al. 2010) for which the maximum is
273 typically reached between 1300 LT and 1600 LT. Prior studies (e.g. Bechtold et al.
274 2004; Guichard et al. 2004; Dai 2006; Rio et al. 2009; 2012) have documented the
275 presence of an afternoon peak in land region precipitation, especially in the tropics, in
276 observations, cloud resolving models (CRM). Most current GCMs tend to produce
277 rainfall too early in the day, thereby contributing to errors and biases in the energy
278 budgets at the surface and at the top of the atmosphere (TOA).

279

280 As illustrated in Fig 1c, for continental RCE, approximate equilibrium exists in terms of
281 daily averages while the instantaneous (or subdaily) atmosphere is not strictly in a RCE
282 state. That is, over the course of the day, the atmospheric column experiences daytime
283 net warming that is compensated by nighttime net cooling. Fig 1d depicts contributions
284 to atmospheric column energy budget from atmospheric absorption of incoming
285 shortwave solar radiation and emitted terrestrial longwave radiation, surface sensible
286 heating, and latent heating by condensation/precipitation. The diurnal cycle of the
287 surface energy budget resembles its atmospheric counterpart, with heating during the
288 day and cooling at night. However, the maximum soil heating occurs early in the
289 morning, when turbulent fluxes are still not very intense and cannot dissipate much of
290 the energy excess (i.e. net surface radiative heating); rather, most of the heating is
291 dissipated as ground heat flux (Gentine et al. 2011; 2012). In terms of hydrologic cycle,
292 the daily-averaged precipitation and evaporation balance each other with surface
293 precipitation in different simulations ranging from about 1 to about 3 mm/day
294 (discussed below).

295

296 Fig 1d depicts the diurnal evolution of radiative cooling and convective heating
297 integrated over the atmospheric column. Convective heating exhibits a strong diurnal
298 cycle imposed by the large-amplitude diurnal variations in surface turbulent heat fluxes.
299 The radiative cooling is simultaneously decreased (in absolute value) and becomes
300 positive between 9 and 15 local time because of the large shortwave attenuation
301 induced by deep convective anvils. Diurnal variations in longwave radiative cooling are
302 an order of magnitude smaller than the shortwave component.

303

304 3. Existence of multiple equilibria

305

306 The sensitivity of RCE to changes in solar forcing, total moisture and initial surface
307 temperature is investigated by modifying 3 parameters: the latitude λ , the total water
308 content Q_{tot} , and the initial ground temperature T_{soil} . The latitude and total water content,
309 with ranges of $\lambda = [30^\circ: 32.5^\circ: 35^\circ: 37.5^\circ: 40^\circ]$ and Q_{tot}
310 $= [5\text{mm}: 15\text{mm}: 25\text{mm}: 35\text{mm}: 45\text{mm}]$, respectively, may be regarded as proxies for
311 different climatic conditions. The initial ground temperature is varied over the range T_{soil}
312 $= [280\text{K}: 290\text{K}: 300\text{K}: 310\text{K}: 320\text{K}]$. A total of 125, 10-year simulations were performed,
313 with other model parameters set to the baseline case values. In what follows, we
314 describe each simulation's final state by its mean equilibrium surface temperature T_{soil}
315 (K), soil water content Q_{soil} (mm), and precipitable water PRW(mm). Note that for a
316 given latitude and total water content, multiple equilibria are present if the distinct final
317 states are achieved with different initial ground temperatures.

318

319 Before discussing the sensitivity analysis, we point out that a strong negative correlation
320 exists between equilibrium surface temperature and soil moisture content, since the
321 evapotranspiration coefficient β increases with soil moisture Q_{soil} . Low Q_{soil} generates
322 low evaporation, so most of the net radiative heating at the surface must be balanced by
323 sensible heat flux (ground heat flux or sensible heat flux). On the other hand, latent
324 heat release is a more efficient heat transfer mechanism than longwave radiation,
325 sensible and ground heat flux (Bateni and Entekhabi 2012). In the absence of
326 substantial soil moisture the surface temperature therefore strongly rises since latent

327 heat flux provides little cooling. Such behavior is well-known for the daily variations of
328 surface skin temperature (Bastiaanssen et al. 1998; Castelli et al. 1999) but it is
329 interesting to point out that the negative correlation between soil moisture and surface
330 temperature also holds at equilibrium.

331

332 Fig 2 provides an overview of the RCE combinations of λ , Q_{tot} , and initial T_{soil} . No
333 multiple equilibria are present at either high or low latitude, or equivalently, high or low
334 solar radiation: that is, at $\lambda = 30^\circ$ ($\lambda = 40^\circ$) the RCE is warm (cold). The warm RCE
335 corresponds to a mean surface temperature $T_s \approx 310$ K and to a dry surface, while the
336 cold RCE corresponds to a mean surface temperature $T_s \approx 273$ K and dry atmosphere.

337 Apart from those extreme latitudes multiple equilibria are found in almost all other
338 conditions. The multiple equilibria appear to be either bimodal or trimodal. For a given
339 total moisture, increasing the latitude increases the possibility of cold RCE states. This
340 is particularly remarkable at $Q_{tot} = 30$ mm, at this point a latitude increase leads to a
341 monotonic increase of final soil temperature/humidity of the cold states. The leftward
342 shift of the warm states also indicates that the warm RCE solutions cool with increased
343 latitude. We should point out that in real climate latitudinal heat transport is very
344 important to mid- and high-latitude climate and is not included in our RCE. This certainly
345 explains why a cold state is already operating at low latitudes with relative high
346 insolation ($\lambda = 40^\circ$) compared to the actual climate.

347

348 Sensitivity to Q_{tot} is nontrivial: at extreme latitudes, the warm RCE state ($\lambda = 30^\circ$) is
349 dependent on total available moisture while the cold state ($\lambda = 40^\circ$) is not. The

350 equilibrium surface T_s increases with Q_{tot} at $\lambda = 30^\circ$, while T_s appears to be quasi-
351 insensitive to variations in Q_{tot} when $\lambda = 40^\circ$ (see Fig 7). At $\lambda = 30^\circ$ the state is “water-
352 limited”: TOA radiation is large and generates important surface evaporation so that the
353 soil is nearly entirely dessicated. The internal water partitioning between the land and
354 atmosphere needs to be such to avoid complete surface water depletion. At high
355 latitudes ($\lambda = 40^\circ$) nearly all available water in the system resides in the soil, with the
356 atmosphere almost entirely devoid of moisture. This corresponds to an “energy-limited”
357 regime: TOA insolation is insufficient to generate substantial surface latent heat release,
358 a more efficient energy consuming process than sensible heat release (Gentine et al.
359 2010; Bateni and Entekhabi 2012). At this altitude, varying Q_{tot} produces little difference
360 in atmosphere, as PRW remains constant. Thus, the radiative properties of the
361 atmosphere, and consequently the equilibrium surface temperature, are invariant with
362 respect to Q_{tot} .

363

364 A warm, dry-surface state is observed when $\lambda = 30^\circ$. In these situations a warm
365 equilibrium exists with all water residing in the atmosphere; the surface temperature for
366 this state is ~ 25 K higher than the other state. This difference is associated with a
367 difference in the cloud cover vertical distribution at equilibrium. Hotter surface
368 temperatures are associated with the presence of higher cloud cover at high altitudes.
369 Those high-level clouds introduce a downwelling longwave forcing at TOA (Bony et al.
370 2004; Bony and Dufresne 2005; Bony et al. 2006) which heats the atmosphere and the
371 surface.

372

373 For intermediate latitudes, increasing Q_{tot} generates intermediate equilibrium states, in
374 which water is more equitably partitioned between the soil and the atmosphere. Two
375 equilibria are present when $Q_{tot} = 50\text{mm}$. In this case the system either falls into a
376 warm (clear) or cold (cloudy) RCE. However, the RCE becomes more multimodal when
377 increasing Q_{tot} . Rather than converging towards distinct equilibrium states, the coupled
378 system tends towards groups of 2 or 3 RCE states for which surface temperature and
379 precipitable water are close but not exactly the same. Consideration of cloud cover
380 vertical profiles (Fig. 3) indicates that these intermediate states are characterized by the
381 presence of at least 2 cloud layers: in addition to the high cloud layer, i.e. the deep
382 convective anvil top, there is a low cloud layer, which corresponds to the development
383 of a shallow cumulus layer prior to deep convective onset. For $Q_{tot} = 60\text{ mm}$ and Q_{tot}
384 $= 70\text{ mm}$, a third cloud layer appears just above the surface. This cloud layer
385 corresponds to morning mist or fog occurring between 0300 LT and 0900 LT (see Fig 3
386 - with the MIST emphasize near the surface).

387

388 The intermediate RCE states occur under intermediate latitude and total moisture
389 conditions: that is, to realize such states, the system must be in neither an energy- nor
390 water-limited regime. Indeed, at high latitudes, the atmosphere is so cold that a low
391 saturation point leads to large relative humidity, in turn inducing large cloud cover that
392 maintains the system into a cold state. Moreover, insolation is insufficient to evaporate
393 surface water and heat the atmosphere through water vapor absorption of longwave
394 radiation. In conclusion, we note here an “optimum” range of λ (energy) and Q_{tot} (water)
395 values that allow intermediate states with neither a completely dry, desert-like, nor fully

396 wet, swamp-like, surface. This range corresponds to a regime that is neither “energy-
397 limited” (in terms of solar radiation) nor “water-limited” (in terms of total water content).
398 Within this range, the coupled land-atmosphere SCM system exhibits multimodal RCE
399 states.

400

401 4. Investigation of equilibria states (dry, wet and 402 intermediate)

403

404 *4a. Surface*

405 In the warm and dry state, surface temperature reaches approximately 310 K and all the
406 water evaporates into the atmosphere, as seen in Fig 2. Again we point out the
407 importance of the system’s finite water quantity for determining the characteristics of
408 this RCE state. Convection in this state is not very intense, but most precipitation that
409 does fall is convective in nature.

410

411 To understand the occurrence of the dry and warm-surface state, we note that with
412 abundant soil moisture, surface latent heat flux is a more efficient mechanism for
413 cooling the surface than sensible heat flux because of the large latent heat of
414 vaporization (Bateni and Entekhabi 2012). In the case of small (soil) moisture the
415 surface turbulent heat fluxes and outgoing surface radiation are insufficient to balance
416 the surface incoming radiation. The resultant energy imbalance at the surface is then
417 dissipated as ground heat flux, which warms the deep soil temperature. This deep soil

418 temperature progressively feeds back on and warms the surface temperature, which
419 helps further evaporate the soil moisture. If total moisture is small, moisture in the
420 atmosphere is insufficient to induce the necessary albedo to fully mitigate the warming
421 through increased cloud cover. The surface ultimately dries up leading to the warm and
422 dry surface state.

423

424 We briefly remark on this state's intriguing transient behavior, namely the system is
425 found to pass through a stage during the first four years of the simulation that is distinct
426 from the long-term equilibrium (not shown). Even though this intermediate state is
427 relatively steady (in an annual-mean sense), it is metastable rather than absolutely
428 stable. During this stage, the system experiences large quasi-periodic (~ 6 month)
429 fluctuations, with the atmosphere oscillating between cold, cloudy and warm, clear
430 regimes.

431

432 In the cold and surface-humid state, the equilibrium mean surface temperature is about
433 273 K, with precipitation removing most water from the atmosphere (only 5 mm of
434 precipitable water is present). The RCE results in a quasi-dry atmosphere, with low
435 precipitation and convection. Large scale precipitation is induced by the large relative
436 humidity at around 800hPa, suggesting that large-scale condensational heating is
437 required to balance the radiative cooling.

438

439 For the intermediate RCE states, equilibrium surface temperature varies from 280 to
440 300 K and water is present in both the soil and the atmosphere. In this case, convective

441 strength is maximized, with precipitation $\sim 2x$ larger than in the other two cases (not
442 shown). At higher latitudes, $\lambda = 40^\circ$, surface insolation is small, while atmospheric
443 relative humidity is large resulting from the large moisture content and low temperature.
444 Surface radiation is small and evaporation is consequently small. Little moisture is
445 hence supplied to the atmosphere. Indeed at low temperatures latent heat release is not
446 effective compared to radiative and sensible heat dissipation (Bateni and Entekhabi
447 2012).

448

449 ***4b. Convective and radiative profiles***

450 The RCE vertical atmospheric profiles, depicted in Fig 4, provide some insight into the
451 physical processes important for maintaining the RCE states. The heating tendencies
452 (Fig 4a) reveal some key features of RCE states, including the strength and depth of
453 convection. Except for the high latitude cases, RCE holds at any height in the vertical,
454 that is, deep convection compensates radiative losses at each level: however, for λ of
455 37.5° and 40° , large-scale diabatic processes occur in the lower layer extending from
456 the surface to 700 hPa, (not shown) thereby compensating radiative tendencies along
457 with those from deep convection.

458

459 It is interesting to point out that some RCE solutions may manifest similar behavior in a
460 vertically-averaged sense, but with very different vertical heating profiles (e.g. Lat= 30° -
461 32.5° - 35°). The principal differences in the radiative heating vertical distribution among
462 the different equilibria, and thus in the convective heating profiles, are readily seen in
463 the vertical extent of the radiative convective instability, with convection height and

464 strength increasing with latitude. This result is consistent with the monotonic increase of
465 the average surface temperature with latitude, which exerts a strong control on
466 convection depth via control of the moist adiabatic temperature profile (Larsson &
467 Hartmann, 2005). Larsson and Hartmann (2005) argue that the altitude where radiative
468 cooling drops to zero determines the anvil top, i.e., the cloud top detrainment zone.
469 Differences in convection heights are quite considerable between the cold case (300
470 hPa) and the warm case (150 hPa).

471

472 ***4c. Cloud cover***

473 The vertical distribution of cloud fraction depicted in Fig 4b reveals important differences
474 between the different RCE states. Fig 5 further emphasizes the diurnal cycle of cloud
475 cover. Cloud fraction increases monotonically with latitude. Low-level clouds are
476 completely absent in at the lowest latitude, while some are present at intermediate
477 latitudes. Cloud top decreases with latitude, in agreement with the decreasing vertical
478 extent of moist convection. In intermediate states a cloud layer is present just above the
479 surface, which corresponds to a morning “fog” or “mist” layer. This layer represents
480 distinct behavior from an oceanic boundary, since it is generated by rapid nocturnal
481 cooling of the surface, which leads to condensation as seen in Fig 5. This condensed
482 layer is thus mostly induced by diurnal evolution of the surface energy budget, unlike
483 stratocumuli over the ocean, which are induced through a combination of surface latent
484 heat flux, a shallow boundary layer, and large-scale subsidence.

485

486 In the cold case, by contrast, two strong peaks are present in the vertical profile of cloud
487 fraction: the lowest peak extends from 900 hPa to 700 hPa and corresponds to a
488 stratocumulus layer with a very large cloud fraction. This layer is generated in the SCM
489 by large-scale condensation, which is triggered by the high relative humidity (>90%) in
490 this layer. This cloud layer is opaque to longwave radiation (Wood 2012), explaining the
491 strong radiative cooling peak near the cloud top (750 hPa). This dense cloud layer also
492 traps longwave radiation in the lower atmosphere, leading to net radiative heating
493 around 950 hPa (Figure 4, upper left). The second peak in cloud cover occurs much
494 higher, between 500 hPa and 250 hPa, and corresponds to the anvil cloud top. This
495 cloud layer exerts less influence on the radiative heating profile than the lower cloud
496 layer, which indicates that the clouds are optically thin. This cloud layer corresponds to
497 cirrus clouds generated via detrainment at the cumulonimbus top. Such clouds are more
498 frequently observed over continents than oceans (Rossow and Schiffer 1999). We
499 should point out that the model does not include the latent heat of melting, which could
500 bias the cirrus generation. When decomposing the radiative tendencies into a
501 shortwave and longwave component, most of the differences are explained by the
502 longwave component (not shown), and are mostly a function of cloud vertical
503 distribution.

504

505 The decrease of cloud top altitude with latitude is clearly visible in Fig 4 and 5. During
506 the daytime, cloud amount is maximized because of moist convection. The diurnal
507 progression from shallow to deep convection is apparent in all cases: shallow clouds
508 appear in the morning, deepen, and ultimately transition to precipitating cumulonimbus.
509 Once deep convection is triggered, heavy rainfall and associated cold pools fed by

510 unsaturated downdrafts tend to cool and stabilize the boundary layer (Tompkins
511 2001a,b; Grandpeix et al. 2010; Grandpeix and Lafore 2010). This stabilization likely
512 accounts for the sudden disappearance of low-level clouds in the mid-afternoon in the
513 warm cases, despite the fact that convective precipitation is still present. Indeed, the
514 time lag between low and high level clouds illustrates the succession between shallow
515 and deep convective regimes.

516

517 Large differences in cloud cover are also observed between the 3 equilibrium states, as
518 seen in Fig.3 and 4. In the cold state, two thick cloud layers are permanent (based on
519 analysis of the diurnal cycle not shown here), i.e., the system is locked into a very stable
520 regime. This stable, cloudy state has been found in other studies using SCMs such as
521 the CFMIP-GASS Intercomparison of LES and SCM models (CGILS) (Zhang et al.
522 2012), which sought to enhance understanding of the transition from stratocumulus to
523 cumulus regimes. Brient (2011) found that adding stochastic noise to the vertical motion
524 field greatly improved the SCM's capacity to mimic the observed cloud cover vertical
525 distribution. This suggests that maintaining a constant vertical wind velocity (here 0) as
526 is the case here may favor "locked" cloudy regimes in SCMs.

527

528 Differences in cloud cover are evident between the intermediate and the warm state in
529 as seen Fig. 3 and 4. The significant difference is the existence of the near surface fog
530 layer between 0300 LT and 0900 LT in the intermediate state (not shown), which is not
531 present in the warm state as emphasized in Fig 5. However, this condensed layer plays
532 a very important role in cooling the lower atmosphere by reflecting incoming sunlight at

533 the surface. This mist layer not only cools the surface but also delays (by ~2 hours) the
534 deepening of the boundary layer, thereby modulating the entire diurnal cycle of deep
535 convection. We also point to the shorter duration of convective events in the warm case,
536 as seen in Figure 5: high clouds peak from 14-18LT, while in the cold case high clouds
537 with a larger cloud fraction peak from 10am all the way until 2 am.

538

539 ***4d. Humidity profile and precipitation***

540 Interestingly, in terms of relative humidity profiles, the cold equilibrium state is more
541 humid, although there is much less precipitable water than in other cases (Fig. 6). At the
542 cumulonimbus top, relative humidity always exceeds 50%. Of course, the atmosphere is
543 so cold that the saturation level is very low. Again, relative humidity clearly distinguishes
544 the three equilibrium states. RH profiles also clearly show the increase of the deep
545 convection top with decreasing latitude (Figure 4c).

546

547 Consideration of the vertical profiles of precipitation points to the source of the
548 maximum surface rain observed in Fig 4d for the intermediate state. In particular, the
549 vertical structure suggests a tradeoff between cloud base precipitation and rain re-
550 evaporation beneath cloud base. With increasing insolation, the vertical profile of
551 convective heating shifts upward and strengthens: thus, the maximum rainfall rate at
552 cloud base occurs at the lowest latitude. On the other hand, since the lower atmosphere
553 is very dry at this latitude, the rain rate drops dramatically in the subcloud layer. As a
554 consequence, surface precipitation is modest at the lowest latitude. With increasing
555 latitude, the below cloud re-evaporation weakens. Taken together, the cloud-base rain

556 intensity and subcloud re-evaporation produce the observed nonmonotonic behavior of
557 surface precipitation.

558

559 We also note that, in general, evaporative cooling occurring at lower levels largely
560 compensates condensational warming of the upper atmosphere. Ultimately, this
561 explains the equivalent vertical integral of the convective heating observed in Fig 4. In
562 summary, convection strengthens as latitude decreases but boundary layer deepening
563 and drying enhances evaporative cooling in the lower atmosphere. This strong
564 evaporating cooling fuels very intense unsaturated downdrafts that spread at the
565 surface as density currents (not shown).

566

567 To summarize the results thus far, we have shown that coupled land-atmosphere
568 system under RCE tends to fall into preferred states (i.e. attractors), i.e., for $T_0=280$ K
569 and $Q_{tot}=60$ mm, the system has 3 preferred states for 5 different latitudes. Clouds and
570 their interaction with radiation, such as the mist layer observed above, may play a key
571 role in the establishment of these equilibrium states, through their nonlinear interaction
572 with radiation.

573

574 5. Role of diurnal cycle and cloud radiative feedback on 575 multiple equilibria

576

577 The relative importance of clouds and of the diurnal cycle for the emergence of multiple
578 equilibria is now evaluated. Two sets of sensitivity experiments for the range of Q_{tot} and
579 T_{soil} values at $\lambda = 35^\circ$ were performed, the first one removing the diurnal cycle and the
580 second one removing cloud radiative forcing, i.e., clouds were rendered transparent to
581 both shortwave and longwave radiation. The RCE states for these sensitivity
582 experiments are plotted in Fig 6. Removing the diurnal cycle strongly reduces the
583 likelihood of obtaining multiple equilibria, while removing the cloud radiative almost
584 completely eliminates multiple equilibria, at least for the conditions considered here.
585 When removing the cloud radiative effect, the system has a single stable state and the
586 equilibrium surface temperature is about 300 K for all Q_{tot} .

587
588 Fig. 7 emphasizes the role of the different cloud types: low- and high-level. In these
589 experiments only the radiative effect of one type of cloud is held and the other clouds
590 are made transparent to radiation. The no cloud and high-cloud experiment exhibit very
591 similar behavior so that high-cloud do not seem to be the main source of nonlinearity
592 and multiple equilibria. No multiple equilibria are found in the high-level cloud case and
593 no-cloud case. The introduction of the low-level radiation feedback leads to multiple
594 equilibria very similar to the full-fledge simulation with both low- and high-level clouds.
595 Therefore we conclude that with our model low-level clouds are the main source of
596 nonlinearity leading to multiple equilibria. This further emphasize the important role of
597 the mist layer observed above and its coupling with the diurnal cycle so that the surface
598 temperature falls below dew temperature. Low-level clouds are known to be the main

599 source of GCM spread (Bony et al. 2004; Bony and Dufresne 2005; Bony et al. 2006)
600 and their importance is further emphasized here over continents.

601
602 Thus, clouds appear to be a critical element for system nonlinearity, with the diurnal
603 cycle providing the internal variability that allows the system to explore different RCE
604 states. In the presence of interactive clouds, the RCE states correspond to distinct cloud
605 vertical distributions as shown in Figure 3. Via feedbacks associated with convection,
606 clouds and radiative cooling, some convective regimes may be favored rather than
607 others. That is, clouds strongly modulate the radiative cooling profiles with which the
608 convective heating profiles must adjust to obtain RCE. In turn, vertical mixing of energy
609 and moisture induced by moist convection ultimately leads to cloud formation, which
610 affects radiation.

611
612 One may certainly question the model-dependence of these results. While a full
613 exploration of this issue is beyond the scope of the present study, we performed
614 analogous sensitivity experiments with the version of the LMDZ GCM used for the 4th
615 IPCC assessment (AR4) (Hourdin 2006). In almost all cases, the RCE states in the
616 older generation model are single, clearly separated states. Significantly, no low level
617 clouds are present in these simulations. Indeed, Hourdin (2006) pointed out that an
618 important bias of the AR4 version of the LMDZ GCM was its inability to represent low-
619 level clouds (i.e. cumulus and stratocumulus). At first glance, these results implicate
620 low-level clouds as necessary for obtaining multiple equilibria.

621

622 6. Summary and conclusions

623

624 In this study we have examined the applicability of RCE over a land surface using a
625 single column atmosphere version of the LMDZ GCM coupled to an idealized land
626 surface model. Relative to its oceanic counterpart, the land system has a finite moisture
627 capacity corresponding to the initial total water content in the soil and in the atmosphere
628 since atmospheric transport and runoff are neglected, i.e., the hydrologic cycle is locally
629 closed. Over the ranges of latitude and total water content explored, multiple equilibria
630 can be obtained by varying initial soil temperature. Three classes of states are possible,
631 namely i) a warm and dry surface with most of the system water content residing in the
632 atmosphere; ii) an intermediate state with water present both in the soil and in the
633 atmosphere; and iii) a cold and wet surface with nearly no moisture present in the
634 atmosphere.

635

636 By considering sensitivity experiments in which boundary layer diurnal cycle and cloud
637 radiative forcing are disabled, we show how these are necessary for the occurrence of
638 multiple equilibria in the LMDZ SCM and how they determine the characteristics of the
639 final state equilibrium. In particular, low-level clouds and mist are key for the presence
640 of multiple equilibria. For low Q_{tot} the system is bimodal and intermediate RCEs are not
641 possible. Increasing Q_{tot} allows multimodal equilibria with partitioning of water both in
642 the soil and in the atmosphere. These intermediate states correspond to two- or three-
643 layer cloud fraction distributions. In the two-layer case succession of shallow and deep
644 convection during daytime creates successively cumulus and anvil clouds. In the three-

645 layer case a morning mist takes place before shallow convection onset. Above a
646 threshold value for Q_{tot} , multiple equilibria are not possible anymore and the system falls
647 into a cold state. High relative humidity then favors the presence of a permanent, thick
648 layer of low-level clouds. Out of this latitude range either all the water evaporates (low
649 latitude warm states), corresponding to a water-limited regime, or precipitates (high
650 latitude cold states), corresponding to an energy-limited regime. Overall our results
651 indicate the key role of the diurnal cycle of the surface temperature and boundary layer,
652 as well as low-level clouds for the final equilibria of the land-atmosphere system.

653

654 **Acknowledgements**

655 Benjamin R. Lintner and Pierre Gentine would like to acknowledge support from NSF
656 Grant NSF-AGS 1035843: Collaborative Research: Quantifying the Impacts of
657 Atmospheric and Land Surface Heterogeneity. Adam H Sobel acknowledges funding
658 from Grant NSF AGS-1008847. The authors would like to thank Christoph Schär and
659 Bjorn Stevens for stimulating discussions of this work.

660

661

662

663

REFERENCES:

664

665 Aleina, F. C., M. Baudena, F. D'Andrea, and A. Provenzale, 2013: Multiple equilibria on planet
666 Dune: climate–vegetation dynamics on a sandy planet. *Tellus B*, **65**, 693,
667 doi:10.1029/2006RG000217.

668 Bastiaanssen, W. G. M., M. Menenti, R. A. Feddes, and A. A. M. Holtslag, 1998: A remote
669 sensing surface energy balance algorithm for land (SEBAL) - 1. Formulation. *J Hydrol*, **212-**
670 **213**, 198–212, doi:10.1016/S0022-1694(98)00253-4.

671 Bateni, S. M., and D. Entekhabi, 2012: Relative efficiency of land surface energy balance
672 components. *Water Resour Res*, **48**, W04510–, doi:10.1029/2011WR011357.

673 Bechtold, P., J. Chaboureau, A. Beljaars, A. K. Betts, M. Kohler, M. J. Miller, and J.
674 Redelsperger, 2004: The simulation of the diurnal cycle of convective precipitation over land
675 in a global model. *Q J Roy Meteor Soc*, **130**, 3119–3137, doi:10.1256/qj.03.103.

676 Betts, A. K., 1973: Non-precipitating cumulus convection and its parameterization. *Q J Roy*
677 *Meteor Soc*, **99**, 178–196.

678 Betts, A. K., 1976: The Thermodynamic Transformation of the Tropical Subcloud Layer by
679 Precipitation and Downdrafts. *Journal of Atmospheric Sciences*, **33**, 1008–1020,
680 doi:10.1175/1520-0469.

681 Bony, S. and Coauthors, 2006: How well do we understand and evaluate climate change
682 feedback processes? *J Climate*, **19**, 3445–3482.

683 Bony, S., and J. Dufresne, 2005: Marine boundary layer clouds at the heart of tropical cloud

684 feedback uncertainties in climate models. *Geophys Res Lett*, **32**, L20806,
685 doi:10.1029/2005GL023851.

686 Bony, S., and K. A. Emanuel, 2001: A parameterization of the cloudiness associated with
687 cumulus convection; Evaluation using TOGA COARE data. *J Atmos Sci*, **58**, 3158–3183.

688 Bony, S., J. L. Dufresne, H. Le Treut, J. J. Morcrette, and C. Senior, 2004: On dynamic and
689 thermodynamic components of cloud changes. *Clim Dynam*, **22**, 71–86,
690 doi:10.1007/s00382-003-0369-6.

691 Brubaker, K., and D. Entekhabi, 1995: An analytic approach to modeling land atmosphere
692 interaction 1. Construct and equilibrium behavior. *Water Resour Res*, **31**, 619–632.

693 Castelli, F., D. Entekhabi, and E. Caporali, 1999: Estimation of surface heat flux and an index of
694 soil moisture using adjoint-state surface energy balance. *Water Resour Res*, **35**, 3115–3125.

695 Dai, A., 2006: Precipitation characteristics in eighteen coupled climate models. *J Climate*, **19**,
696 4605–4630.

697 DelSole, T., M. Zhao, and P. A. Dirmeyer, 2009: A New Method for Exploring Coupled Land-
698 Atmosphere Dynamics. *J Hydrometeorol*, **10**, 1040–1050, doi:10.1175/2009JHM1071.1.

699 Derbyshire, S., I. Beau, P. Bechtold, J. Grandpeix, J. Piriou, J. Redelsperger, and P. M. M.
700 Soares, 2004: Sensitivity of moist convection to environmental humidity. *Q J Roy Meteor*
701 *Soc*, **130**, 3055–3079, doi:10.1256/qj.03.130.

702 Emanuel, K. A., 1991: A Scheme for Representing Cumulus Convection in Large-Scale Models.
703 *J Atmos Sci*, **48**, 2313–2335.

704 Entekhabi, D., and K. Brubaker, 1995: An analytic approach to modeling land-atmosphere

705 interaction, 2, Stochastic formulation. *Water Resour Res*, **31**, 633–643.

706 Entekhabi, D., I. Rodríguez-Iturbe, and R. L. Bras, 1992: Variability in Large-Scale Water-
707 Balance with Land Surface Atmosphere Interaction. *J Climate*, **5**, 798–813.

708 Findell, K., P. Gentine, and B. Lintner, 2011: Probability of afternoon precipitation in eastern
709 United States and Mexico enhanced by high evaporation. *Nat Geosci*, **4**, 434–439,
710 doi:10.1038/NGEO1174.

711 Gentine, P., A. A. M. Holtslag, F. D'Andrea, and M. Ek, 2013: Surface and atmospheric controls
712 on the onset of moist convection over land. *J Hydrometeorol*, 130211131121003,
713 doi:10.1175/JHM-D-12-0137.1.

714 Gentine, P., B. Heusinkveld, and D. Entekhabi, 2012: Systematic Errors in Ground Heat Flux
715 Estimation and Their Correction. *Water Resour Res*, **48**, W09541,
716 doi:10.1029/2010WR010203.

717 Gentine, P., D. Entekhabi, and J. Polcher, 2010: Spectral Behaviour of a Coupled Land-Surface
718 and Boundary-Layer System. *Bound-Lay Meteorol*, **134**, 157–180, doi:10.1007/s10546-009-
719 9433-z.

720 Gentine, P., J. Polcher, and D. Entekhabi, 2011: Harmonic propagation of variability in surface
721 energy balance within a coupled soil-vegetation-atmosphere system. *Water resources*
722 *Research*, **47**, –, doi:10.1029/2010WR009268.

723 Grandpeix, J. Y., and V. Phillips, 2004: Improved Mixing Representation in Emanuel's
724 Convection Scheme. *Q J Roy Meteor Soc*, **130**, 3207–3222, doi:10.1256/qj.03.144.

725 Grandpeix, J.-Y., and J.-P. Lafore, 2010: A Density Current Parameterization Coupled with
726 Emanuel's Convection Scheme. Part I: The Models. *J Atmos Sci*, **67**, 881–897,

727 doi:10.1175/2009JAS3044.1.

728 Grandpeix, J.-Y., J.-P. Lafore, and F. Cheruy, 2010: A Density Current Parameterization
729 Coupled with Emanuel's Convection Scheme. Part II: 1D Simulations. *J Atmos Sci*, **67**, 898–
730 922, doi:10.1175/2009JAS3045.1.

731 Guichard, F. and Coauthors, 2004: Modelling the diurnal cycle of deep precipitating convection
732 over land with cloud-resolving models and single-column models. *Q J Roy Meteor Soc*, **130**,
733 3139–3172, doi:10.1256/qj.03.145.

734 Guo, Z. and Coauthors, 2006: GLACE: The Global Land-Atmosphere Coupling Experiment. Part
735 II: Analysis. *J Hydrometeorol*, **7**, 611–625.

736 Hohenegger, C., P. Brockhaus, C. S. Bretherton, and C. Schaer, 2009: The Soil Moisture-
737 Precipitation Feedback in Simulations with Explicit and Parameterized Convection. *J*
738 *Climate*, **22**, 5003–5020, doi:10.1175/2009JCLI2604.1.

739 Hourdin, F., F. Couvreux, and L. Menut, 2002: Parameterization of the dry convective boundary
740 layer based on a mass flux representation of thermals. *J Atmos Sci*, **59**, 1105–1123.

741 Hourdin, F., J. Y. Grandpeix, C. Rio, S. Bony, and A. Jam, 2012: LMDZ5B: the Atmospheric
742 Component of the IPSL Climate Model with Revisited Parameterizations for Clouds and
743 Convection. *Clim Dynam*, doi:10.1007/s00382-012-1343-y.

744 Koster, R. D. and Coauthors, 2006: GLACE: The Global Land-Atmosphere Coupling Experiment.
745 Part I: Overview. *J Hydrometeorol*, **7**, 590–610.

746 Koster, R. D., and M. J. Suarez, 1994: The Components of a Svat Scheme and Their Effects on
747 a Gcms Hydrological Cycle. Vol. 17 of, *Advances in Water Resources*, 61–78.

748 Laio, F., A. Porporato, L. Ridolfi, and I. Rodríguez-Iturbe, 2001: Plants in water-controlled
749 ecosystems: active role in hydrologic processes and response to water stress - II.
750 Probabilistic soil moisture dynamics. *Adv Water Resour*, **24**, 707–723.

751 Manabe, S., and R. T. Wetherald, 1967: Thermal equilibrium of the atmosphere with a given
752 distribution of relative humidity. *The Warming Papers: The Scientific Foundation for the*
753 *Climate Change Forecast*, 94–115.

754 Muller, C. J., P. A. O’Gorman, and L. E. Back, 2011: Intensification of Precipitation Extremes
755 with Warming in a Cloud-Resolving Model. *J Climate*, **24**, 2784–2800,
756 doi:10.1175/2011JCLI3876.1.

757 Porporato, A., F. Laio, L. Ridolfi, and I. Rodríguez-Iturbe, 2001: Plants in water-controlled
758 ecosystems: active role in hydrologic processes and response to water stress - III.
759 Vegetation water stress. *Adv Water Resour*, **24**, 725–744.

760 Renno, N., 1997: Multiple equilibria in radiative-convective atmospheres. *Tellus Series A-*
761 *Dynamic Meteorology And Oceanography*, **49**, 423–438.

762 Rio, C., and F. Hourdin, 2008: A thermal plume model for the convective boundary layer:
763 Representation of cumulus clouds. *J Atmos Sci*, **65**, 407–425, doi:10.1175/2007JAS2256.1.

764 Rio, C., F. Hourdin, F. Couvreux, and A. Jam, 2010: Resolved Versus Parametrized Boundary-
765 Layer Plumes. Part II: Continuous Formulations of Mixing Rates for Mass-Flux Schemes.
766 *Bound-Lay Meteorol*, **135**, 469–483, doi:10.1007/s10546-010-9478-z.

767 Rio, C., F. Hourdin, J. Y. Grandpeix, and J. P. Lafore, 2009: Shifting the diurnal cycle of
768 parameterized deep convection over land. *Geophys Res Lett*, **36**, –,
769 doi:10.1029/2008GL036779.

770 Rio, C., J. Y. Grandpeix, F. Hourdin, and F. Guichard, 2012: Control of deep convection by sub-
771 cloud lifting processes: the ALP closure in the LMDZ5B general circulation model. *Clim*
772 *Dynam*, 2271–2292.

773 Rodríguez-Iturbe, I., A. Porporato, L. Ridolfi, V. Isham, and D. R. Cox, 1999: Probabilistic
774 modelling of water balance at a point: the role of climate, soil and vegetation. *P R Soc A*,
775 **455**, 3789–3805.

776 Rodríguez-Iturbe, I., D. Entekhabi, and R. L. Bras, 1991a: Nonlinear Dynamics of Soil-Moisture
777 at Climate Scales .1. Stochastic-Analysis. *Water resources Research*, **27**, 1899–1906.

778 Rodríguez-Iturbe, I., D. Entekhabi, J. LEE, and R. L. Bras, 1991b: Nonlinear Dynamics of Soil-
779 Moisture at Climate Scales .2. Chaotic Analysis. *Water resources Research*, **27**, 1907–1915.

780 Romps, D. M., 2011: Response of Tropical Precipitation to Global Warming. *J Atmos Sci*, **68**,
781 123–138, doi:10.1175/2010JAS3542.1.

782 Rossow, W. B., and R. A. Schiffer, 1999: Advances in understanding clouds from ISCCP. *Bull.*
783 *Amer. Meteor. Soc*, **80**, 2261–2287.

784 Schlemmer, L., C. Hohenegger, J. Schmidli, C. S. Bretherton, and C. Schaer, 2011: An
785 Idealized Cloud-Resolving Framework for the Study of Midlatitude Diurnal Convection over
786 Land. *J Atmos Sci*, **68**, 1041–1057, doi:10.1175/2010JAS3640.1.

787 Seneviratne, S. I., T. Corti, E. L. Davin, M. Hirschi, E. B. Jaeger, I. Lehner, B. Orlowsky, and A.
788 J. Teuling, 2010: Investigating soil moisture-climate interactions in a changing climate: A
789 review. *Earth-Sci Rev*, **99**, 125–161, doi:10.1016/j.earscirev.2010.02.004.

790 Simpson, J., and V. Wiggert, 1969: Models of Precipitating Cumulus Towers. *Mon Wea Rev*, **97**,
791 471–489.

792 Tompkins, A. M., 2001a: Organization of Tropical Convection in Low Vertical Wind Shears: The
793 Role of Water Vapor. *J Atmos Sci*, **58**, 529–545, doi:10.1175/1520-0469(2001)058.

794 Tompkins, A. M., 2001b: Organization of Tropical Convection in Low Vertical Wind Shears: The
795 Role of Cold Pools. *J Atmos Sci*, **58**, 1650–1672, doi:10.1175/1520-0469(2001)058.

796 Tompkins, A. M., and G. C. Craig, 1998a: Time-scales of adjustment to radiative-convective
797 equilibrium in the tropical atmosphere. *Q J Roy Meteor Soc*, **124**, 2693–2713,
798 doi:10.1002/qj.49712455208.

799 Tompkins, A. M., and G. C. Craig, 1998b: Radiative–convective equilibrium in a three-
800 dimensional cloud-ensemble model. *Q J Roy Meteor Soc*, **124**, 2073–2097,
801 doi:10.1002/qj.49712455013.

802 Wood, R., 2012: Stratocumulus Clouds. *Mon Wea Rev*, **140**, 2373–2423, doi:10.1175/MWR-D-
803 11-00121.1.

804 Zhang, M., C. S. Bretherton, and P. N. Blossey, 2012: The CGILS experimental design to
805 investigate low cloud feedbacks in general circulation models by using single-column and
806 large-eddy simulation models. *Journal of Advances in Modeling Earth Systems-Discussion*,
807 **4**, doi:10.1029/2012MS000182.

808

809

810

811

812
813
814
815
816
817
818
819
820
821
822
823
824
825
826
827
828
829
830
831
832
833
834
835
836
837

FIGURE CAPTION LIST:

Fig 1: Averaged diurnal cycle over the last 3 months of : a) Upper left: Surface temperature, b) Upper right: Surface precipitation. Lat=35°, $T_o=300$ K and $Q_{tot}=40$ mm, c) Lower left: Top of the atmosphere solar forcing (dashed), atmosphere energy balance (green), surface energy balance (purple) and surface turbulent fluxes (red), d) Lower right: Convective heating (red), Radiative heating (blue) decomposed in its short wave (circle line) and long wave (dashed lines) components,

Fig 2: Average surface temperature T_{sol} (K) versus soil water content Q_{sol} (kg/m²) (and precipitable water (kg/m²) $PRW = Q_{tot} - Q_{sol}$) over the last 3 months for different latitudes (from left to right Lat = [30°,32.5°,35°,37.5°,40°]), total water content (from up to bottom $Q_{tot} = [30,40,50,60,70]$ (kg/m²)) and initial ground temperatures ($T_o = [280$ (blue), 290 (light blue), 300 (green), 310 (purple), 320 (red)])

Fig 3: Average vertical profiles of the cloud fraction over the last 3 months for different latitudes (from left to right Lat = [30°,32.5°,35°,37.5°,40°]), total water content (from up to bottom $Q_{tot} = [30,40,50,60,70]$ (kg/m²)) and initial ground temperatures ($T_o = [280$ (blue), 290 (light blue), 300 (green), 310 (purple), 320 (red)])

Fig 4: Mean vertical profile over the lasts 3 months of convective (solid lines) and radiative (dashed lines) heating (upper left), cloud fraction (upper right), relative humidity (lower left) and precipitation (lower right). Large scale tendencies are not taken into account. Latitudes are 30° (red), 32.5° (pink), 35° (green), 37.5° (light blue), 40° (blue). Initial ground temperature is $T_o=280$ K and total water is $Q_{tot}=60$ mm

Fig 5: Mean diurnal cycle of the cloud fraction over the last 3 months for different latitudes. Initial ground temperature is $T_o=280$ K and total water is $Q_{tot}=60$ mm

838 Fig 6: Average surface temperature T_{sol} (K) versus soil water content Q_{sol} (kg/m² or mm) (and precipitable
839 water (kg/m²) $PRW = Q_{tot} - Q_{sol}$) over the last 3 months for $Lat=35^\circ$, different total water content (from up
840 to bottom $Q_{tot} = [30,40,50,60,70]$ (mm)) and initial ground temperatures ($T_o = [280$ (blue), 290 (light blue),
841 300 (green), 310 (purple), 320 (red)])

842

843 Fig 7: Time series of daily mean surface temperature (top left), soil water content (upper right), convective
844 (solid lines) and stratiform dashed lines precipitation (lower left), and precipitable water (lower right).
845 Latitudes are 30° (red), 32.5° (pink), 35° (green), 37.5° (light blue), 40° (blue). Initial ground temperature
846 is $T_o=280$ K and total water is $Q_{tot}=60$ mm

847

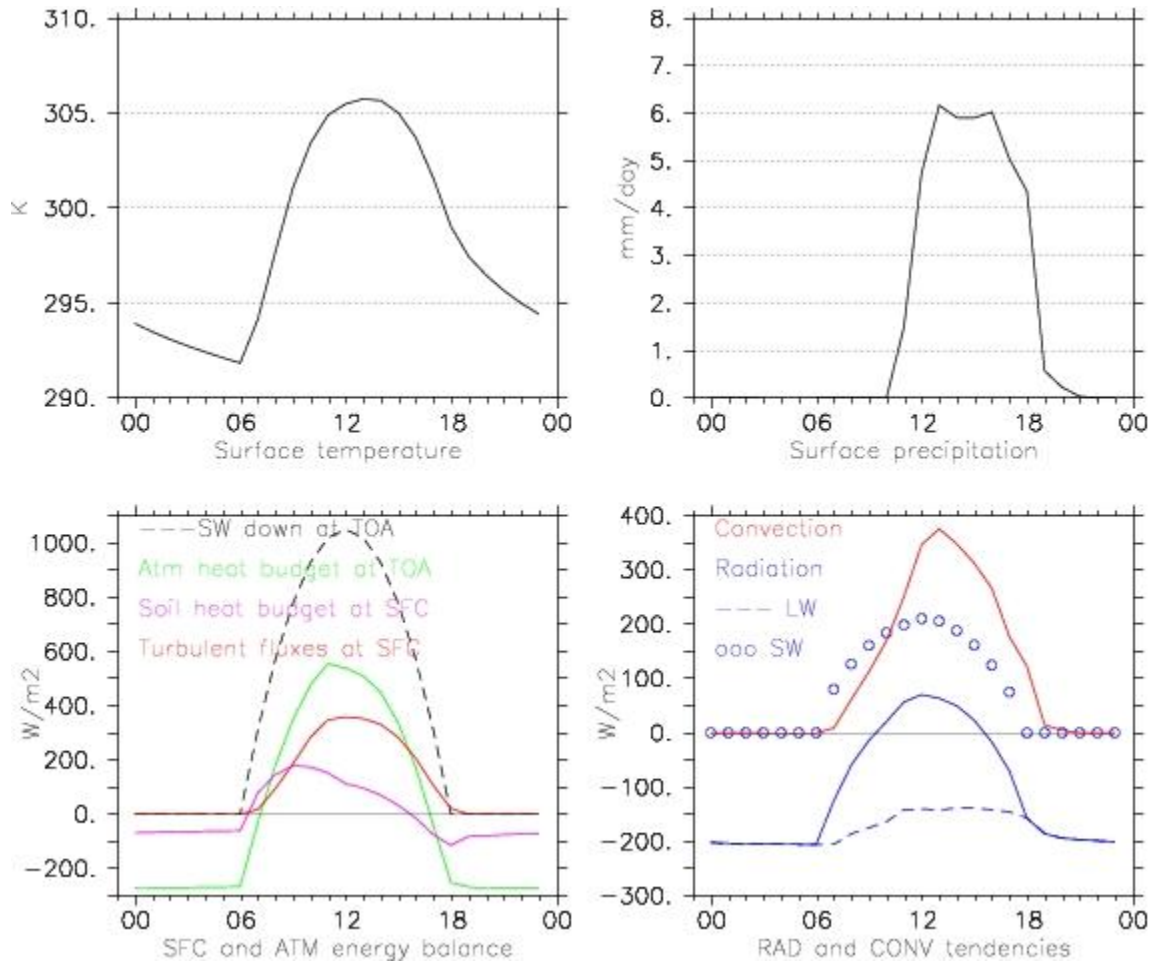
848

849

850

851
852
853

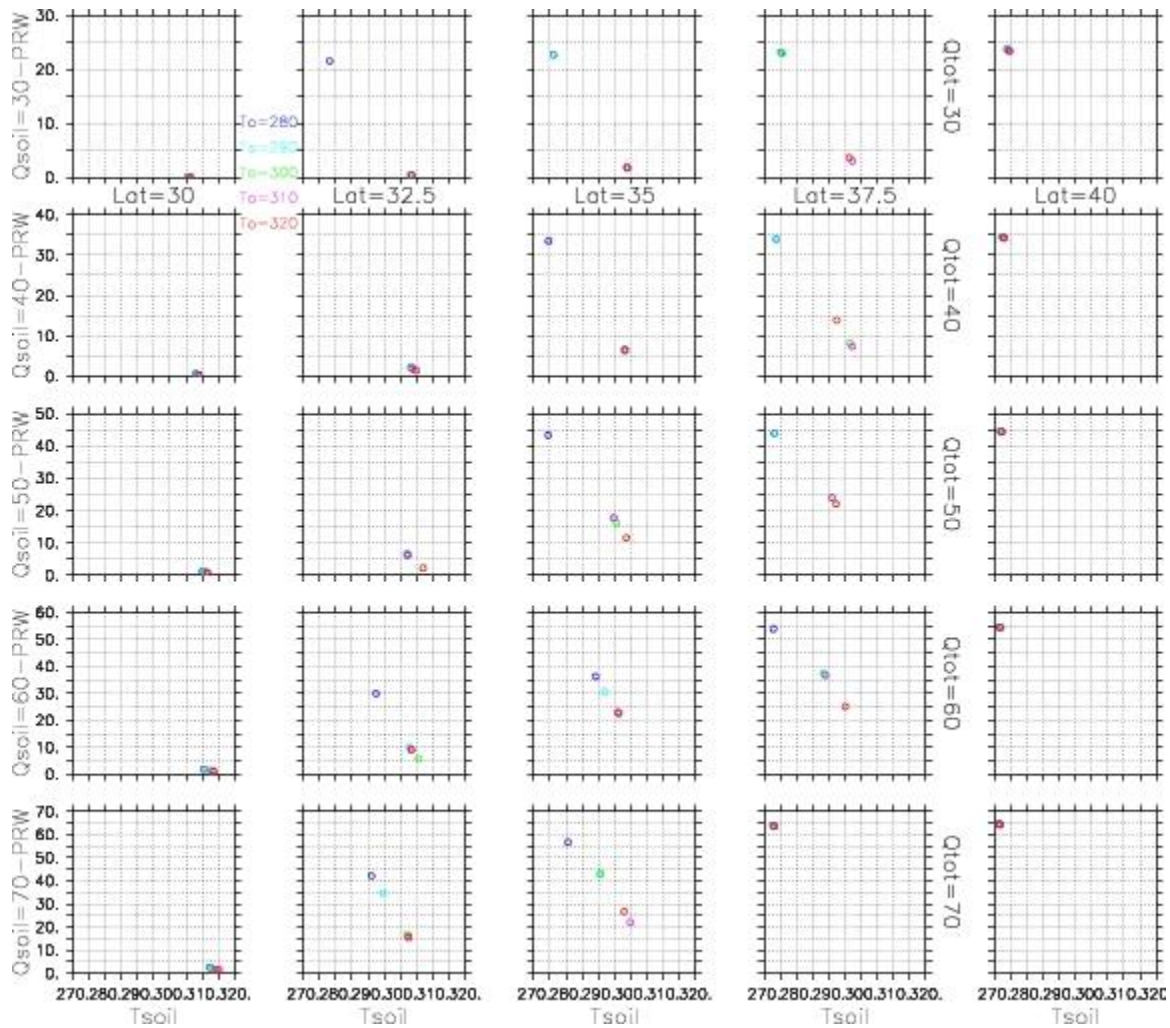
FIGURES:



854
855
856
857
858
859
860
861
862

Fig 1: Averaged diurnal cycle over the last 3 months of : a) Upper left: Surface temperature, b) Upper right: Surface precipitation. Lat=35°, $T_o=300$ K and $Q_{tot}=40$ mm, c) Lower left: Top of the atmosphere solar forcing (dashed), atmosphere energy balance (green), surface energy balance (purple) and surface turbulent fluxes (red), d) Lower right: Convective heating (red), Radiative heating (blue) decomposed in its short wave (circle line) and long wave (dashed lines) components,

863

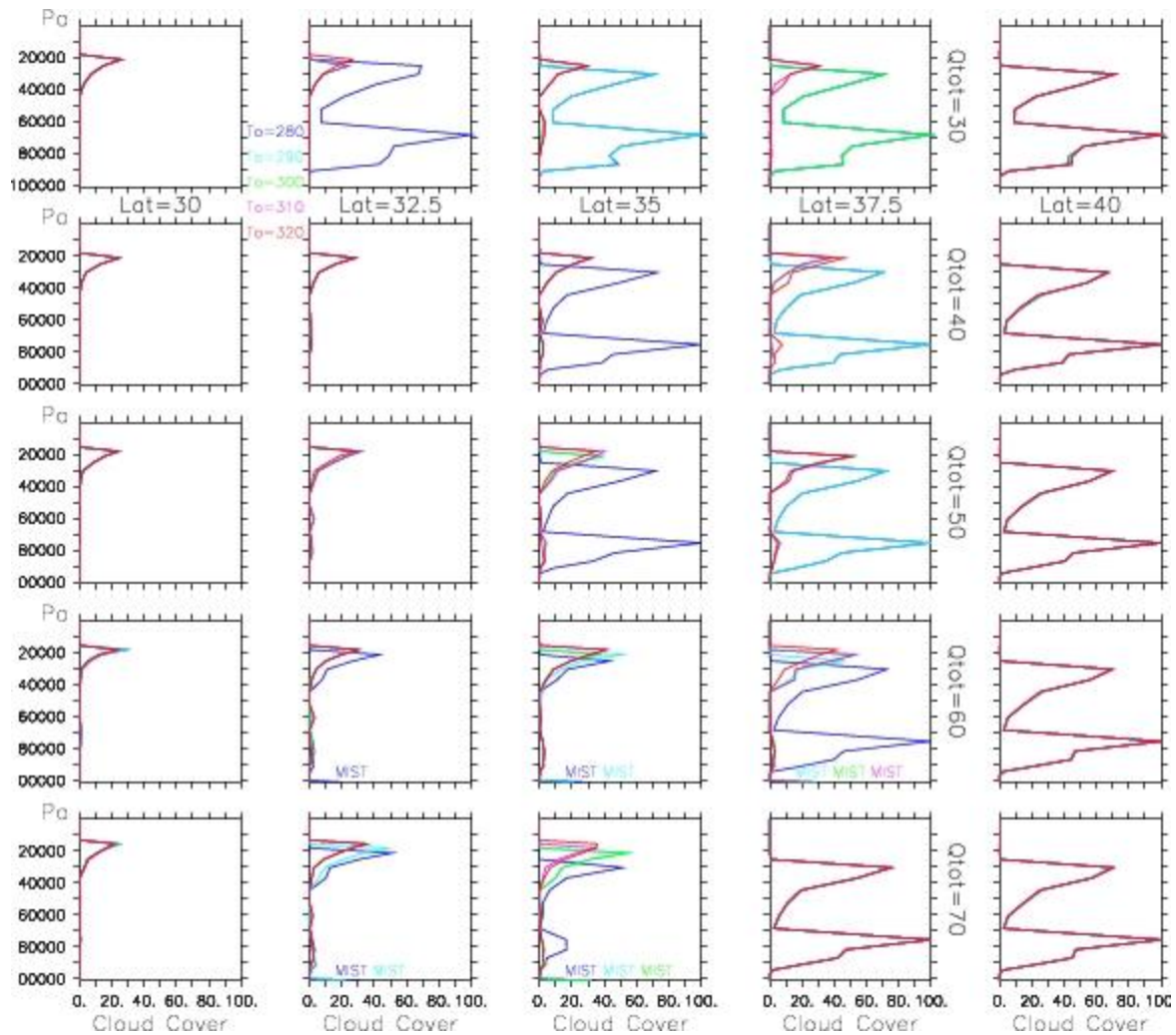


864

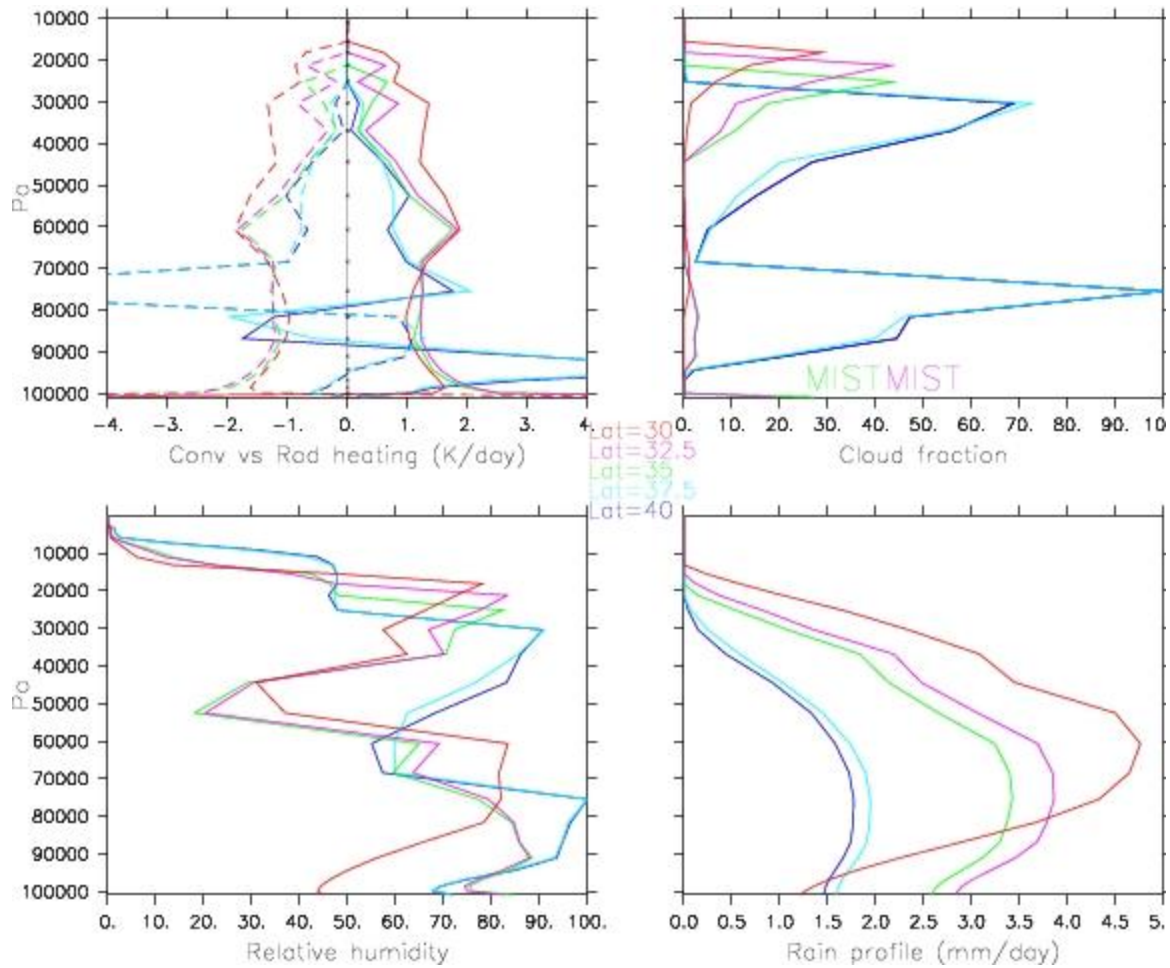
865 Fig 2: Average surface temperature T_{sol} (K) versus soil water content Q_{sol} (kg/m^2) (and precipitable water
866 (kg/m^2) $\text{PRW} = Q_{tot} - Q_{sol}$) over the last 3 months for different latitudes (from left to right $\text{Lat} =$
867 $[30^\circ, 32.5^\circ, 35^\circ, 37.5^\circ, 40^\circ]$), total water content (from up to bottom $Q_{tot} = [30, 40, 50, 60, 70]$ (kg/m^2)) and initial
868 ground temperatures ($T_o = [280$ (blue), 290 (light blue), 300 (green), 310 (purple), 320 (red)])

869

870



871
 872 Fig 3: Average vertical profiles of the cloud fraction over the last 3 months for different latitudes (from left
 873 to right Lat = [30°,32.5°,35°,37.5°,40°]), total water content (from up to bottom Q_{tot} = [30,40,50,60,70]
 874 (kg/m²)) and initial ground temperatures (T_o = [280 (blue), 290 (light blue), 300 (green), 310 (purple), 320
 875 (red)])



876

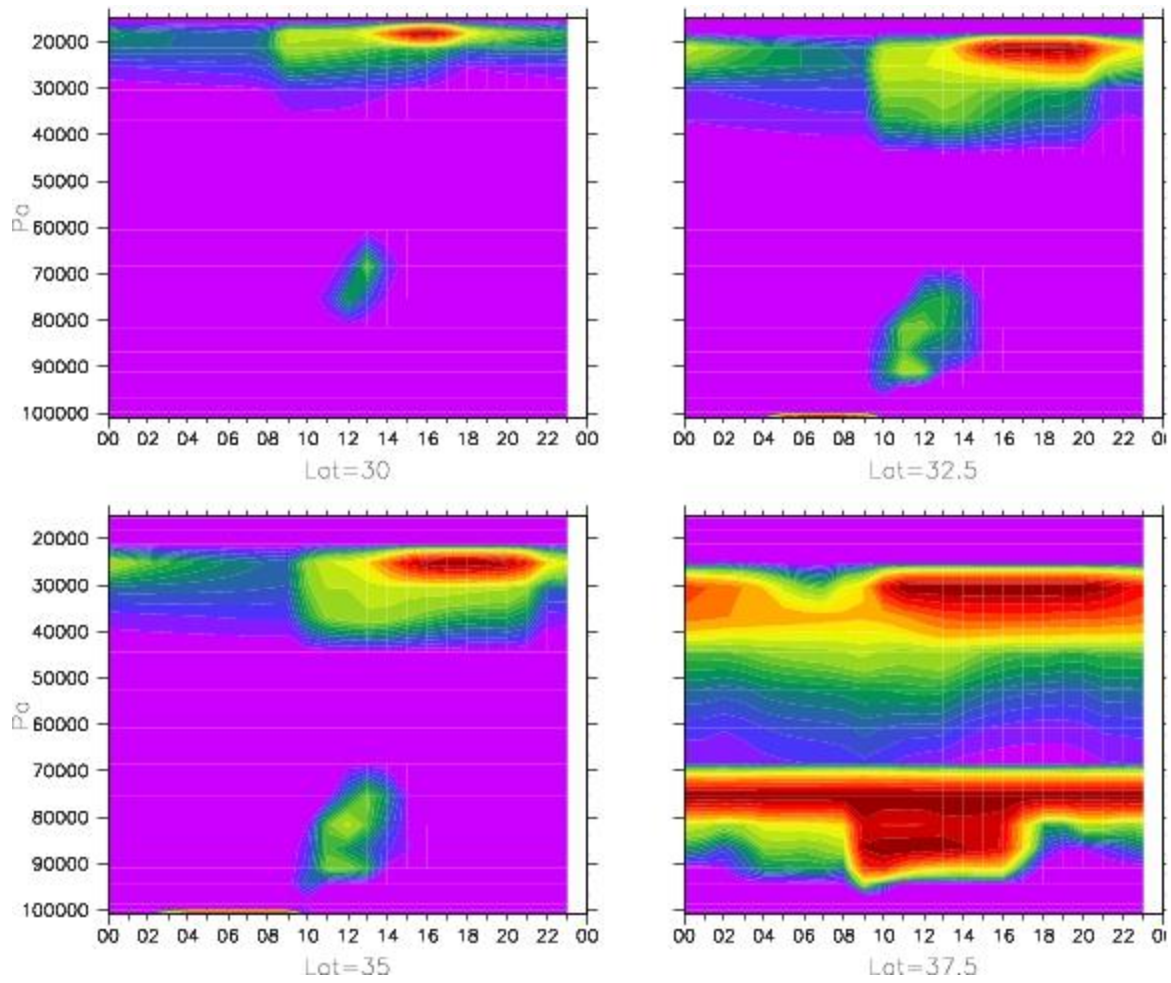
877 Fig 4: Mean vertical profile over the lasts 3 months of convective (solid lines) and radiative (dashed lines)

878 heating (upper left), cloud fraction (upper right), relative humidity (lower left) and precipitation (lower right).

879 Large scale tendencies are not taken into account. Latitudes are 30° (red), 32.5° (pink), 35° (green), 37.5°

880 (light blue), 40° (blue). Initial ground temperature is $T_0=280$ K and total water is $Q_{tot}=60$ mm

881



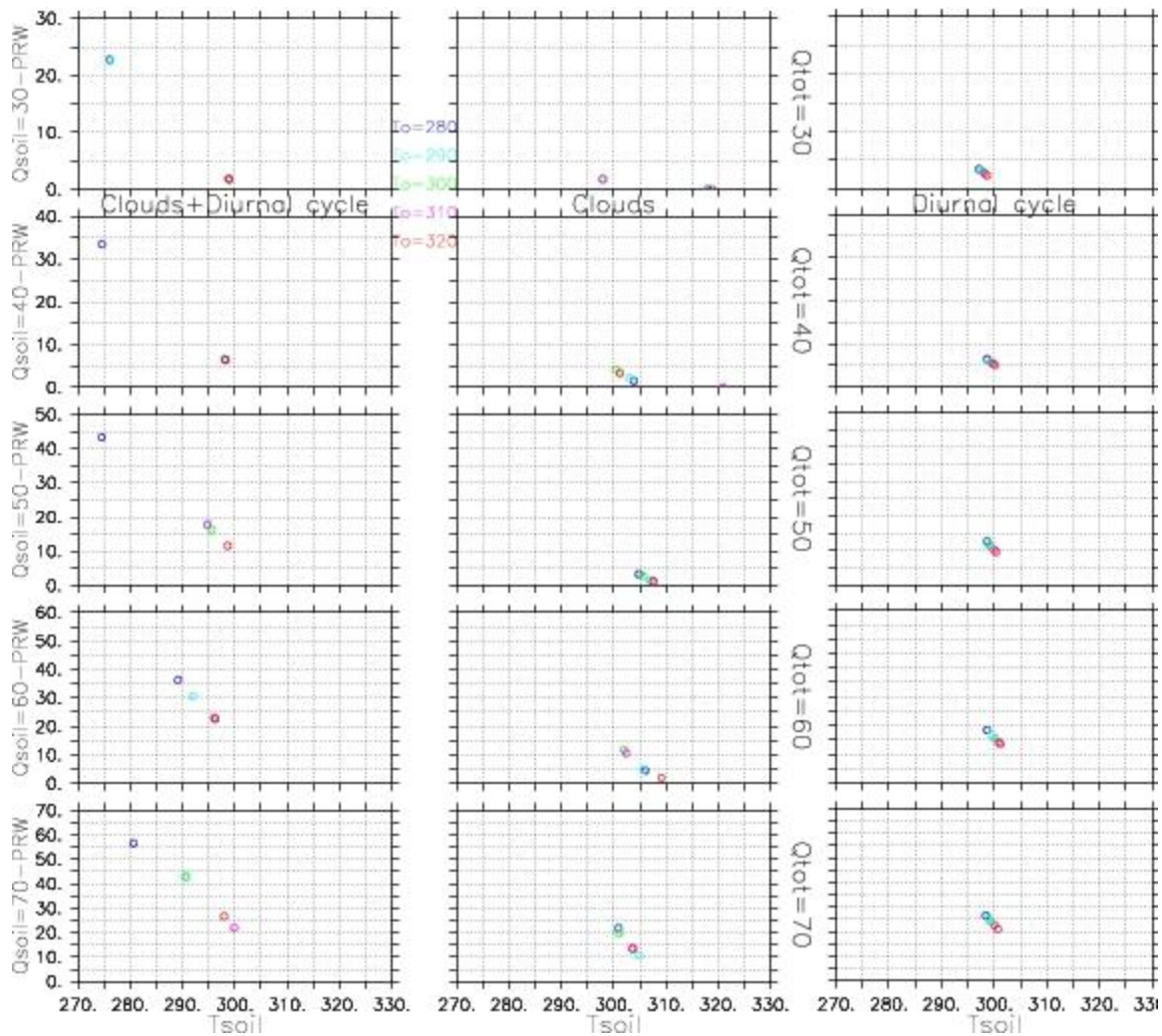
882

883 Fig 5: Mean diurnal cycle of the cloud fraction over the last 3 months for different latitudes. Initial ground

884 temperature is $T_0=280$ K and total water is $Q_{tot}=60$ mm

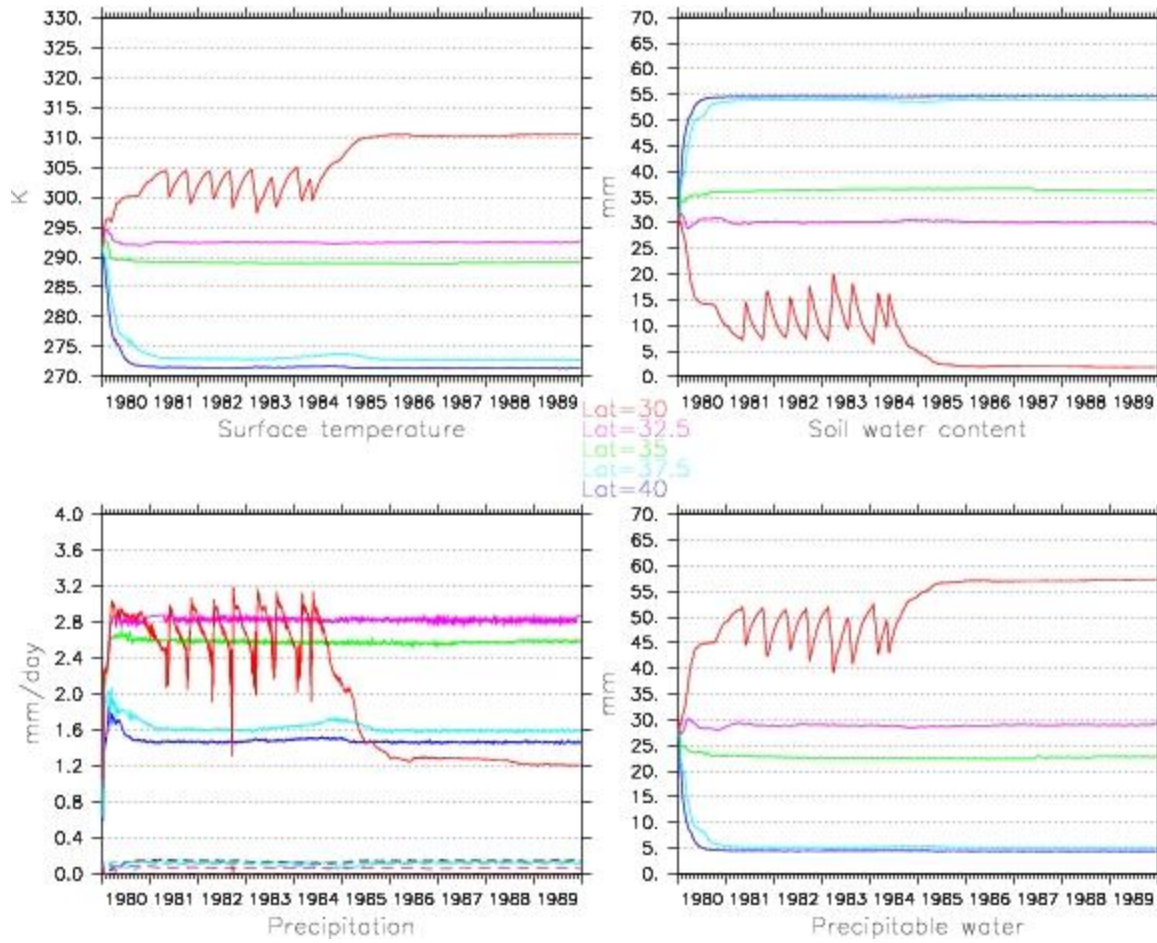
885

886



887

888 Fig 6: Average surface temperature T_{sol} (K) versus soil water content Q_{sol} (kg/m^2 or mm) (and precipitable
 889 water (kg/m^2) $\text{PRW} = Q_{tot} - Q_{sol}$) over the last 3 months for $\text{Lat}=35^\circ$, different total water content (from up
 890 to bottom $Q_{tot} = [30,40,50,60,70]$ (mm)) and initial ground temperatures ($T_o = [280$ (blue), 290 (light blue),
 891 300 (green), 310 (purple), 320 (red)])



892

893 Fig 7: Time series of daily mean surface temperature (top left), soil water content (upper right), convective

894 (solid lines) and stratiform dashed lines precipitation (lower left), and precipitable water (lower right).

895 Latitudes are 30° (red), 32.5° (pink), 35° (green), 37.5° (light blue), 40° (blue). Initial ground temperature

896 is $T_0=280$ K and total water is $Q_{tot}=60$ mm

897

898

899

900